

**Ionization of helium by slow antiproton impact: Total and differential cross sections**S. Borbély,<sup>1,\*</sup> J. Feist,<sup>2,3,4</sup> K. Tórkési,<sup>5</sup> S. Nagele,<sup>4</sup> L. Nagy,<sup>1</sup> and J. Burgdörfer<sup>4,5</sup><sup>1</sup>*Faculty of Physics, Babeş-Bolyai University, 400084 Cluj-Napoca, Romania, EU*<sup>2</sup>*Departamento de Física Teórica de la Materia Condensada, Universidad Autónoma de Madrid, 28049 Madrid, Spain, EU*<sup>3</sup>*ITAMP, Harvard-Smithsonian Center for Astrophysics, Cambridge, Massachusetts 02138, USA*<sup>4</sup>*Institute for Theoretical Physics, Vienna University of Technology, 1040 Vienna, Austria, EU*<sup>5</sup>*Institute for Nuclear Research, Hungarian Academy of Sciences (ATOMKI), H-4026 Debrecen, P.O. Box 51, Hungary, EU*

(Received 4 September 2014; published 10 November 2014)

We investigate theoretically the single and double ionization of the He atom by antiproton impact for projectile energies ranging from 3 keV up to 1000 keV. We obtain accurate total cross sections by directly solving the fully correlated two-electron time-dependent Schrödinger equation. The cross sections are in excellent agreement with the available experimental data. We also present fully *ab initio* doubly differential data for single ionization at 10 and 100 keV impact energies and compare to classical-trajectory Monte Carlo calculations. In these differential cross sections we identify the binary-encounter peak along with the anticusp minimum. Furthermore, we also point out the importance of the postcollisional electron-projectile interaction at low antiproton energies, which significantly suppresses electron emission in the forward direction.

DOI: [10.1103/PhysRevA.90.052706](https://doi.org/10.1103/PhysRevA.90.052706)

PACS number(s): 34.50.Fa, 25.43.+t, 36.10.-k

**I. INTRODUCTION**

The collision of antiprotons with helium atoms is a fundamental process in many-body atomic physics, attracting considerable interest from both the experimental [1–6] and theoretical [6–11] side. This collision system is an ideal candidate to study the four-body Coulomb problem because the number of possible reaction channels is limited: the negative charge of the projectile eliminates the electron-capture channel and, because of the large mass of the projectile, rearrangement processes involving capture of the antiproton by the helium atom are strongly suppressed except at very low energies ( $\sim$ eV).

Up to now, total cross sections for single and double ionization have been measured for impact energies ranging from 3 keV up to a few MeV [1–4]. In addition, singly differential cross sections were measured at 945 keV antiproton impact energy [5]. At high impact energies (above 100 keV) the single ionization (SI) process is predominantly a one-electron process and can be fairly accurately described by using single-active-electron (SAE) approaches [12–14]. However, at lower antiproton impact energies, the simple SAE approaches fail to account for the recent experimental data [3], indicating that SI channels are influenced by two-electron dynamics and correlation effects. This disagreement was, for the most part, resolved by two-active-electron approaches [13–16], which are in relatively good agreement with each other and with the experimental data. Further improvements of the SI and double ionization (DI) cross sections were achieved by extensive *ab initio* calculations using the coupled-pseudostates (CP) [10,17], the convergent close-coupling (CCC) [11], the time-dependent close-coupling (TDCC) [7–9], and the time-dependent density functional theory (TDDFT) [16,18] methods. However, discrepancies between the different approaches remain and call for further investigations (for a comprehensive overview of recent work, see the review by Kirchner and Knudsen [6]).

Except for the work by McGovern *et al.* [10,17] and by Abdurakhmanov *et al.* [11], all recent calculations focused on total ionization cross sections. However, for the design of future differential cross-section measurements [6], predictions for differential ionization cross sections are desirable. Converged *ab initio* calculations for the latter pose a considerable challenge. Motivated by residual discrepancies between different theoretical SI total cross sections and between experiment and theory, and by the need for differential cross sections we performed accurate simulations for total single and double ionization as well as for differential cross sections for single ionization of helium by antiproton impact. We find excellent agreement with experimental data for DI over the entire range of investigated energies ( $3 \text{ keV} \leq E \leq 1 \text{ MeV}$ ) and for SI with the notable exception between 10 and 30 keV. The differential cross sections prominently feature the anticusp minimum and the binary-encounter peak. Atomic units are used unless stated otherwise.

**II. METHOD**

We employ a semiclassical impact-parameter approach where the antiproton moves on a classical straight-line trajectory  $\vec{R}(t) = \vec{b} + \vec{v}_p t$ . Here  $\vec{b}$  is the impact parameter and  $\vec{v}_p$  is the antiproton's velocity. The validity of a classical-trajectory description is well established for energies  $\geq$ keV [6,19]. The de Broglie wavelength  $\lambda_{\vec{p}} = \frac{2\pi}{Mv} \leq 10^{-5}$  is negligibly small compared to the atomic radius of helium. The approximation of the classical trajectory by a straight line was checked by employing classical-trajectory Monte Carlo (CTMC) simulations, where we have calculated the distribution of antiproton trajectories as a function of the scattering angle  $\theta_a$  (i.e., the deviation from the constant-velocity straight-line trajectory). Even for the smallest antiproton energy considered here (3 keV) we obtained a narrow distribution in the forward direction with  $(\theta_a)_{\text{FWHM}} < 2^\circ$ . The validity of the straight-line approximation was also independently verified by other CTMC calculations [20,21].

\*sandor.borbely@phys.ubbcluj.ro

The quantum dynamics of the two active electrons is initiated by the time-dependent Coulomb potential of the incident projectile and is governed by the time-dependent Schrödinger equation (TDSE) which we solve numerically by using the time-dependent close-coupling (TDCC) method [7]. The present implementation is based on a numerical code previously developed for the study of the interaction between a He atom and linearly polarized intense ultrashort laser pulses [22]. Because cylindrical symmetry and the total magnetic quantum number  $M$  are not conserved in antiproton impact, the previous five-dimensional description of the two-electron problem has to be extended to the full six dimensions. The fully correlated two-electron wave function is represented as

$$\Psi(\vec{r}_1, \vec{r}_2, t) = \sum_{l_1 l_2 LM} \frac{R_{l_1 l_2}^{LM}(r_1, r_2, t)}{r_1 r_2} \Upsilon_{l_1 l_2}^{LM}(\Omega_1, \Omega_2), \quad (1)$$

expanded in terms of the symmetrized coupled spherical harmonics

$$\Upsilon_{l_1 l_2}^{LM}(\Omega_1, \Omega_2) = \frac{1}{\sqrt{2 + 2\delta_{M0}}} \left[ Y_{l_1 l_2}^{LM}(\Omega_1, \Omega_2) + (-1)^{l_1 + l_2 + L + M} Y_{l_1 l_2}^{L-M}(\Omega_1, \Omega_2) \right]. \quad (2)$$

We explicitly exploit in Eq. (2) the planar reflection symmetry of the wave function relative to the collisional plane. The radial partial waves  $R_{l_1 l_2}^{LM}(r_1, r_2, t)$  are discretized by using the finite element discrete variable representation (FEDVR) method [23,24], where each radial coordinate is divided into finite elements (FEs) and inside each FE the wave function is represented on a local DVR basis with a corresponding Gauss–Lobatto quadrature to ensure the continuity at the FE boundaries.

For the temporal propagation of the wave function we use the short iterative Lanczos (SIL) method [25,26] with adaptive time-step control. The time evolution operator in each time step is evaluated in the Krylov subspace generated by the repeated action of the Hamiltonian  $\hat{H}$  on the initial state  $\Psi(t)$ . The ground state of helium was obtained by propagating an initial trial wave function in negative imaginary time ( $t \rightarrow -i\tau$ ).

At each impact energy the convergence was carefully checked with respect to the size and density of the FEDVR grid, to the simulated length of the projectile trajectory, and to the size of the angular basis. The radial grid density required for convergence strongly depends on the projectile energy: at 1 MeV, convergence is reached with a radial box of 84 a.u. with 505 grid points (FEDVR order 6), while at 3 keV it required a radial box of 154 a.u. with 481 grid points (order 7). In agreement with previous calculations [7–9,13,14], we find total cross sections have converged for an angular basis with size  $(L, M, l_1, l_2)_{\max} = (3, 3, 3, 3)$ . However, for reaching convergence for differential cross sections we find that a much larger basis size with  $(L, M, l_1, l_2)_{\max} = (5, 5, 5, 5)$  is needed. In all calculations the projectile trajectory was propagated from  $R_z = -40$  a.u. to  $R_z = 80$  a.u. with the position of the helium nucleus at  $R_z = 0$ .

For each impact parameter, the ionization probabilities are extracted from the time-dependent wave function by using the projection onto single and double continuum eigenstates. Since the three- and four-body continuum eigenstates are not

known, we propagate our collision system until the fragments have reached sufficiently large interparticle distances such that electron-electron and electron-projectile interactions can be neglected and final states can be approximated by bound and uncorrelated single, and double continuum eigenstates of a free He atom. Uncorrelated single continuum eigenstates are not orthogonal to the excited bound states. This introduces a significant contamination into the SI spectrum. This contamination is removed by subtracting the numerically obtained exact first few singly excited eigenstates of He with the principal quantum number of the excited electron  $n \leq 7$  from the time-dependent wave function before the calculation of the spectrum. The ionization cross sections are obtained from the ionization probabilities by performing the impact-parameter integration numerically.

The present four-body CTMC approach is based on the numerical solution of the classical Hamilton's equations of motion where all the particles participate in the collision process. The four particles are the antiproton, the helium nucleus, and the two electrons. All particles interact with each other by Coulomb potentials except for the electron pair. Neglecting the latter during the collision is important to suppress unphysical spontaneous autoionization [27]. The two independent, nonequivalent target electrons are initialized according to the microcanonical ensembles with energies corresponding to the first (0.903 a.u.) and second (2 a.u.) ionization potentials, respectively [27]. The impact parameter of the projectile as well as the positions and the velocities of the electrons moving in the field of the target nucleus are randomly selected. The initial conditions of the individual collisions are chosen at sufficiently large internuclear separations such that the interaction between the projectile and the target constituents is negligible. In order to acquire sufficient statistics, we typically propagate  $10^8$  trajectories for each set of collision parameters. The exit channels are identified according to the relative two-body energies determined at large distances (at least  $10^5$  a.u.) from the collision center. This corresponds to an energy resolution of about  $10^{-5}$  a.u. While the four-body CTMC approach lacks predictive quantitative power, it is very helpful in identifying qualitative features in the differential electron distribution and their underlying physical origin.

### III. TOTAL IONIZATION CROSS SECTIONS

Total ionization cross section refers in the following to the cross section integrated over all energies and angles of the emitted electrons. All cross sections (differential and total) discussed in the following are integrated over all impact parameters or, equivalently, all scattering angles  $\theta_a$  of the antiproton. At energies  $\geq 3$  keV the latter are, however, confined to a narrow cone about the forward direction [ $(\theta_a)_{\text{FWHM}} \leq 2^\circ$ ].

To benchmark our present calculations we first compare with antiproton data for total ionization cross sections. In Fig. 1 we compare the present TDCC calculations for the total cross sections for SI at impact energies ranging from 3 keV up to 1 MeV with experimental data measured at CERN by Andersen *et al.* (CERN90) [1], by Hvelplund *et al.* (CERN94) [2], and by Knudsen *et al.* (CERN08) [3]. For improved clarity we split the comparison with various other theoretical results into three subsets. In Fig. 1(a) we compare

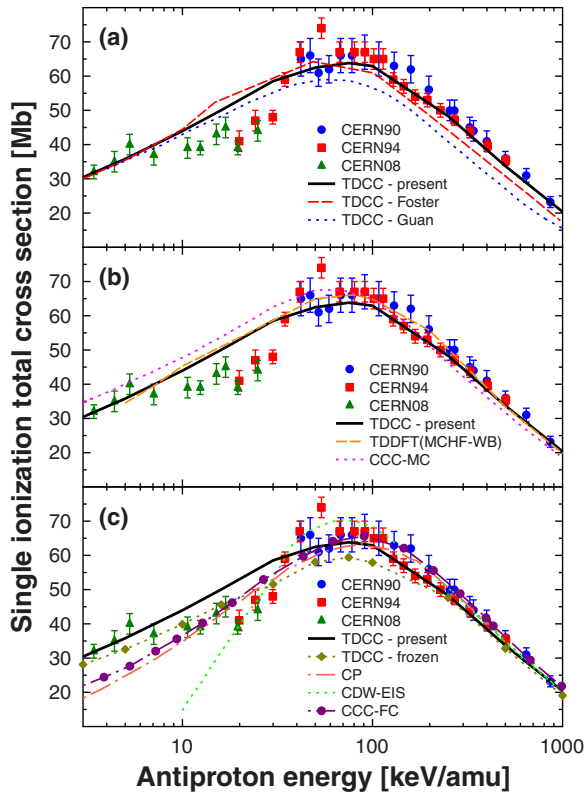


FIG. 1. (Color online) Total ionization cross sections for the single ionization of He by antiproton impact. The present TDCC results are compared with the experimental data of Andersen *et al.* [1] (CERN90), of Hvelplund *et al.* [2] (CERN94), and of Knudsen *et al.* [3] (CERN08). In panel (a) we also compare with the TDDCC results of Foster *et al.* [7,8] (TDCC-Foster) and of Guan *et al.* [9] (TDCC-Guan). In panel (b) we compare with other fully correlated theoretical calculations of Abradurakhmanov *et al.* [11] (CCC-MC) and of Baxter *et al.* [18] (TDDFT). In panel (c) we compare with calculations of McGovern *et al.* [10] (CP), the CDW-EIS calculations [12], the frozen core CCC (CC-FC) calculations [11], and our frozen-TDCC calculations (see text).

with the TDCC data of Foster *et al.* [7,8] and of Guan *et al.* [9], in Fig. 1(b) with the CCC-MC data of Abdurakhmanov [11] and the TDDFT data of Baxter *et al.* [18], and in Fig. 1(c) with the CP data of McGovern [10], the continuum distorted-wave eikonal-initial-state (CDW-EIS) calculations [12], and our frozen-TDCC calculations (explained below).

Our TDCC results show excellent agreement with the experimental data at all studied antiproton impact energies with the notable exception in the 10–30 keV interval where all the experimental data are below our theoretical prediction. At high energies above the Massey maximum [28] at  $\approx 100$  keV we find the closest agreement with the recent TDDFT results of Baxter *et al.* [18] and the CP results of McGovern *et al.* [10] while the TDCC results of Refs. [7–9] appear to underestimate the SI cross sections. The origin of the latter discrepancy is not yet understood. At low energies below the Massey maximum the different TDCC calculations give comparable results, which is not surprising since they are all based on TDCC and employ similar discretization and propagation techniques. Comparing the TDCC with other calculations

including electron correlations at low energies, significant discrepancies appear: the CCC-MC overestimate, while the CP calculations underestimate the TDCC cross sections.

Turning now to the discrepancies of the present TDCC results to experimental data in the energy interval  $10 \text{ keV} \leq E \leq 30 \text{ keV}$  we note that almost all *ab initio* calculations [7–9,11,13–16] display comparable deviations. Notable exceptions are the CDW-EIS calculation of Fainstein *et al.* [12] and partly the CP results of McGovern *et al.* [10]. Both the CP and CDW-EIS methods have in common that they are effective one-electron descriptions, either by invoking a single-active-electron approximation, or by freezing one of two electrons in the  $\text{He}^+(1s)$  state. As also pointed out by Igarashi *et al.* [13] and by Abdurakhmanov *et al.* [11], constraining the dynamics of the second electron (or neglecting it altogether) may lead to an underestimation of the total SI cross section. Additionally, the rapid decrease of the ionization cross section in the CDW-EIS approximation is likely a consequence of the failure of the underlying perturbation approximation at such low ion energies. We inquired into the influence of the suppression of two-electron transitions by performing a TDCC calculation in which we counted only SI events with the bound electron found in the  $1s$  state [frozen-TDCC in Fig. 1(c)]. The total cross section is, indeed, significantly reduced, yielding, most likely, fortuitously good agreement with the experimental data between 10 and 30 keV but an underestimate at high energies. Thus, the discrepancy of the experimental data with the state-of-the-art calculations in the range between 10 and 30 keV remains unresolved and suggests the need for further experimental data in this energy region.

For double ionization (Fig. 2), the present TDCC total cross sections are in excellent agreement with the experimental data over the entire range of antiproton energies considered. The experimental data consist of three sets of Andersen *et al.* [1] (CERN90), Hvelplund *et al.* [2] (CERN94), and Knudsen *et al.* [4] (CERN09). Also, the different TDCC calculations are in close agreement with each other. The improved agreement

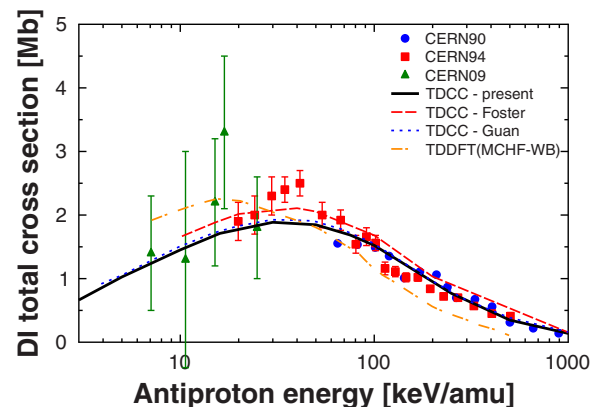


FIG. 2. (Color online) Total ionization cross sections for the double ionization of He by antiproton impact. Experimental data of Andersen *et al.* [1] (CERN90), of Hvelplund *et al.* [2] (CERN94), and of Knudsen *et al.* [4] (CERN09) are compared with the present TDCC and other fully correlated theoretical calculations of Baxter *et al.* [18] (TDDFT), of Foster *et al.* [7] (TDCC-Foster), and of Guan *et al.* [9] (TDCC-Guan).

compared to the SI case suggests that the extraction of *total* double-ionization probabilities from the fully correlated two-electron wave packet is less error prone than the extraction of single-ionization probabilities. Unlike for SI, the discrepancy to the TDDFT calculations [18] is somewhat larger, which may be connected to the difficulty to accurately extract two-particle observables such as DI from a theory that treats only the reduced one-particle density. Clearly, compared to a TDCC approach the TDDFT model has the advantage of a much lower computational cost.

#### IV. DIFFERENTIAL IONIZATION CROSS SECTION

We now turn to the doubly differential (DDCS) and the singly differential (SDCS) cross sections for single ionization of helium. The DDCS can be equivalently expressed in terms of parallel ( $p_{\parallel}$ ) and perpendicular ( $p_{\perp}$ ) electron components relative to the incoming beam direction ( $\hat{v}_p$ ),  $\sigma^{\text{SI}}(p_{\parallel}, p_{\perp})$ , or as energy and angle differential cross section  $\sigma^{\text{SI}}(E_e, \theta)$ . They are related to the total SI cross section by

$$\begin{aligned}\sigma^{\text{SI}} &= \int_{-\infty}^{\infty} dp_{\parallel} \int_0^{\infty} dp_{\perp} \sigma^{\text{SI}}(p_{\parallel}, p_{\perp}) \\ &= \int_0^{\infty} dE_e \int_0^{\pi} d\theta \sin(\theta) \sigma^{\text{SI}}(E_e, \theta).\end{aligned}\quad (3)$$

In Fig. 3 we compare the DDCS  $\sigma^{\text{SI}}(p_{\parallel}, p_{\perp})$  calculated by the present TDCC method and by the classical CTMC simulations. We find good *qualitative* agreement between the TDCC (first row) and CTMC (second row) results. In both models, the differential cross sections display two distinct features. First, at both impact energies the momentum distribution of the

ionized electrons closely follows the binary-encounter ridge (indicated by the half circles) described by the  $2m_e v_p \cos(\theta)$  law of the classical binary-encounter model [29]. Here  $m_e$  is the electron mass,  $v_p$  is the projectile velocity, and  $\theta$  is the electron ejection angle measured from the projectile impact direction. In the binary-encounter model (also referred to as the elastic-scattering model) the ionization process is treated as the elastic scattering of the target electrons at the incoming projectile. Thus, the electrons are emitted with maximum probability when their parallel ( $v_{\parallel}$ ) and perpendicular ( $v_{\perp}$ ) velocity components fulfill the relation

$$v_{\perp}^2 + (v_p - v_{\parallel})^2 = v_p^2. \quad (4)$$

In Eq. (4) the velocity distribution of the target electron (the Compton profile) is neglected. Taking the latter into account yields a velocity distribution centered around Eq. (4). Second, the anticusp [30] is clearly observable as a deep minimum in the forward direction ( $p_{\perp} = 0, p_{\parallel} > 0$ ) when the electron velocity  $v_{\parallel}(= p_{\parallel})$  matches that of the antiproton ( $v_p = v_{\parallel}$ ). For impact energies at and above the Massey maximum (100 keV), similar structures were previously observed by Tókési *et al.* [31] using CTMC and CDW-EIS single-active-electron calculations. At high projectile impact energies the SI ionization is predominantly a single-electron process and the high projectile velocity ensures the validity of the perturbative CDW-EIS approach. The mechanism underlying the formation of the anticusp is simple: the electrons are repelled from the vicinity of the negatively charged projectile by the strong postcollisional Coulomb repulsion. This effect is complementary to the formation of a cusp due to the attractive final-state interactions between the outgoing electron and the positively charged projectile, first observed in the proton-He

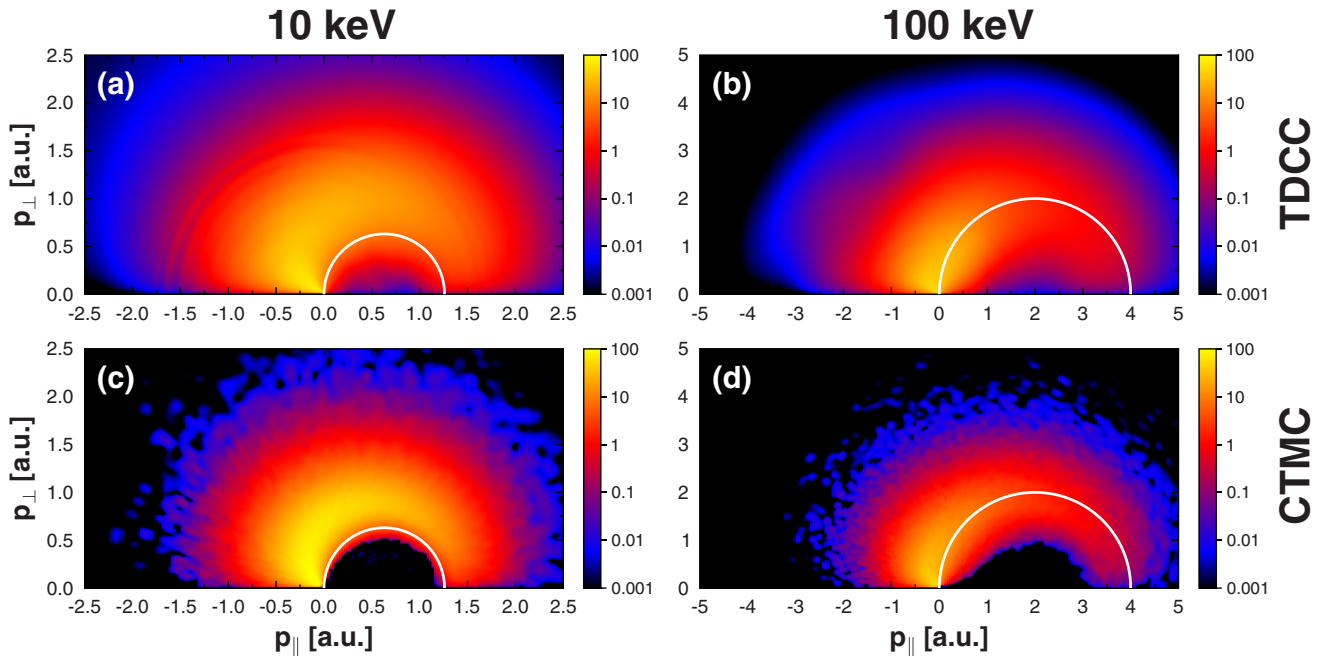


FIG. 3. (Color online) Doubly differential cross section ( $\text{Mb}/\text{a.u.}^2$ ) for SI as a function of the parallel ( $p_{\parallel}$ ) and perpendicular ( $p_{\perp}$ ) momentum components of the ejected electron. (a), (b) TDCC and (c), (d) CTMC calculations are compared at (a), (c) 10 keV and (b), (d) 100 keV antiproton energies. Both models show the characteristic features of the cross sections with the deep anticusp minima around the projectile velocity and the distribution of the continuum electrons around the binary-encounter ridge (half circles); see text.

collisions [32–34]. Both are controlled by the Gamow factor for the two-body final state interaction [31]

$$G(v_{\perp}, v_{\parallel}) = \frac{2\pi |Z_p|}{\sqrt{v_{\perp}^2 + (v_{\parallel} - v_p)^2}} \times e^{\frac{-2\pi |Z_p|}{\sqrt{v_{\perp}^2 + (v_{\parallel} - v_p)^2}}} \quad (Z_p < 0, \text{ repulsive}), \quad (5a)$$

$$G(v_{\perp}, v_{\parallel}) = \frac{2\pi |Z_p|}{\sqrt{v_{\perp}^2 + (v_{\parallel} - v_p)^2}} \quad (Z_p > 0, \text{ attractive}), \quad (5b)$$

where  $Z_p$  is the charge of the projectile. Equation (5) follows from the low-energy limit normalization factor of the two-body Coulomb continuum function [35,36].

The presence of such localized structures in momentum space displaced from the origin raises the question of the convergence of the DDCS in a truncated two-electron angular basis. In order to obtain the Gamow factor in the truncated angular basis we expand the modulus of the normalization factor of the Coulomb continuum function  $\sqrt{G(v_{\perp}, v_{\parallel})}$ ,

$$\sqrt{G(v_{\perp}, v_{\parallel})} = \sum_{l=0}^{\infty} g(v, l) Y_{lm=0}(\theta, \phi = 0), \quad (6)$$

where  $v$  is the electron velocity and  $\theta, \phi$  are the ejection angles. By using the expansion coefficients  $g(v, l)$ , we obtain the Gamow factor in the truncated basis as

$$G(v_{\perp}, v_{\parallel}, l_{\max}) = \left[ \sum_{l=0}^{l_{\max}} g(v, l) Y_{lm=0}(\theta, \phi = 0) \right]^2. \quad (7)$$

Figure 4 presents cuts along the  $v_{\perp} = 0$  and the  $v_{\parallel} = v_p$  planes of the Gamow factor in the truncated angular basis for different maximum angular momenta  $l_{\max}$  for 10 and 100 keV projectile energies. While at low energies the convergence to the Gamow factor is rapid and  $l_{\max} = 1$  is sufficient, at

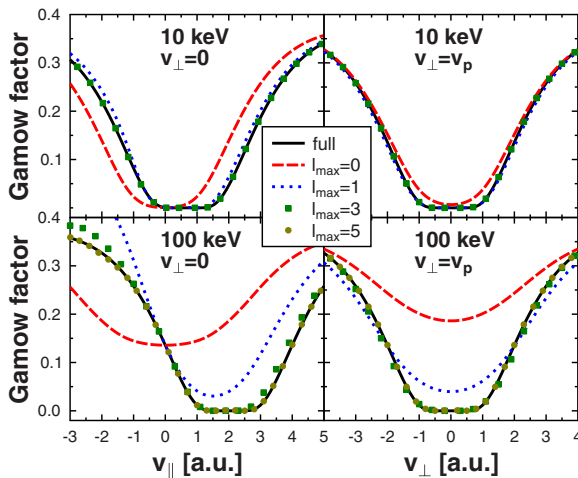


FIG. 4. (Color online) The Gamow factor in the truncated angular basis with maximum angular momentum  $l_{\max}$  for 10 keV (first row) and 100 keV (second row) projectile velocities and cuts along (first column) and perpendicular (second column) to the projectile velocity.

higher energies (100 keV) the structure is so steep that, at the rapidly varying flanks, even  $l_{\max} = 3$  is not sufficient to reach convergence. With  $l_{\max} = 5$  employed in the present TDCC calculation, the Gamow factor in the truncated angular basis coincides with the exact expression within the resolution of the plot. This indicates that our angular basis with  $l_{\max} = 5$  maximum angular momentum is well suited to represent the anticusp. The width in momentum space of the anticusp in the DDCS (Fig. 3) is large at both antiproton energies studied because the continuum electron is repelled in a large region around the vectorial momentum of the antiproton projectile. At 100 keV projectile energy, where the separation between the anticusp minimum and the binary-encounter ridge is large ( $v_p \approx 2$  a.u.), the formation of the anticusp does not significantly influence the electron distribution around the binary-encounter ridge. In contrast, at 10 keV projectile energy ( $v_p \approx 0.63$  a.u.) the anticusp “cuts” into the binary-encounter ridge and “pushes” the ionized electrons out to larger velocities and suppresses emission in the forward direction. In a simple classical picture, the slow projectile facilitates enhanced postcollisional interaction and momentum transfer to the ionized electron. We note that the anticusp is slightly more pronounced in the CTMC calculations than in the TDCC calculations. This effect, only observable on the logarithmic scale (Fig. 3), most likely results from two contributions: for one, exponentially small but finite values of the Gamow factor [Eq. (5a)] represent the tunneling into the classically forbidden regime in coordinate space which, in turn, leads to the suppression of near equivelocity electrons in momentum space. In classical mechanics, the corresponding region in coordinate space is strictly forbidden, translating into a more pronounced hole in momentum space. Second, the quantum calculation may not have sufficiently converged to fully resolve the exponentially suppressed ionization probability when the propagation is terminated at  $R_Z = 80$  a.u. and the residual final-state interaction with the projectile at even larger projectile-target separations is not accounted for.

The singly differential cross section as a function of the emission angle,

$$\sigma^{\text{SI}}(\theta) = \int_0^{\infty} dE \sigma^{\text{SI}}(E, \theta), \quad (8)$$

displays traces of the anticusp in terms of a pronounced minimum near  $\theta = 0^\circ$ , and a maximum in the backward direction  $\theta = 180^\circ$  (Fig. 5). The latter reflects the fact that, in the backward direction, the low-energy ionization spectrum is least affected by the anticusp. In contrast, in the forward direction the electron emission is strongly influenced by the antiproton energy (i.e., by the position of the anticusp). At 100 keV a large fraction of electrons is emitted in the forward direction (see the peak at  $\theta \simeq 60^\circ$ ), which according to Fig. 3(b) are high-energy electrons emitted around the binary-encounter ridge. By lowering the antiproton energy to 10 keV, we observe a significant reduction in the emission of these high-energy forward electrons, which can be also observed in Fig. 3(a) and is the result of the overlap between the binary-encounter ridge and the anticusp minimum. The  $\bar{p} + \text{He}$  system appears therefore as a prime candidate to observe the anticusp, even in SDCS. By comparison, in  $e + \text{He}$  collisions this feature is largely obscured since the

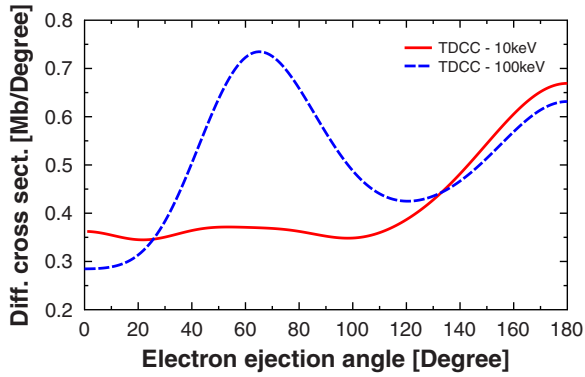


FIG. 5. (Color online) Singly differential cross section  $\sigma^{\text{SI}}(\theta)$  for SI as a function of electron ejection angle.  $\theta = 0^\circ$  corresponds to ejection in the direction of the outgoing antiproton. The figure illustrates the suppression of electron emission in the forward direction for low projectile velocities.

postcollision energy spread of the light projectile smears out the anticusp. For the high projectile energy (100 keV) the binary-encounter ridge near  $60^\circ$  becomes clearly visible.

Since singly differential cross sections may become accessible when future  $\bar{p}$  facilities with larger beam currents come into operation, we also investigate the energy-differential cross section

$$\sigma^{\text{SI}}(E_e) = 2\pi \int_0^{\theta_{\text{max}}} d\theta \sin(\theta) \sigma^{\text{SI}}(E_e, \theta) \quad (9)$$

integrated over all angles within a forward cone up to  $\theta_{\text{max}}$  (Fig. 6). For easier comparison, the SDCSs are normalized

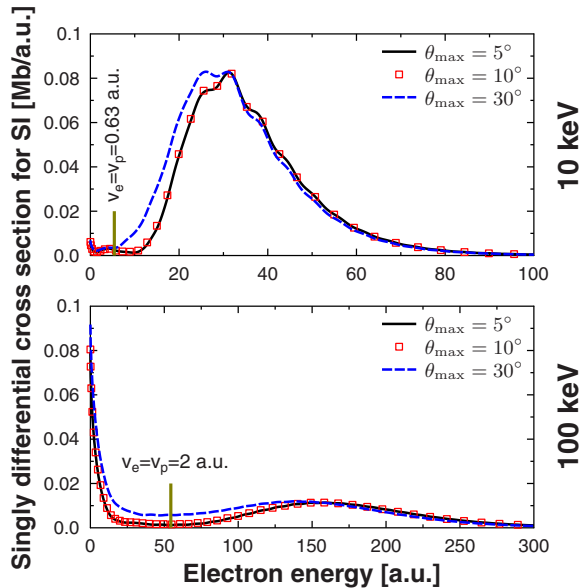


FIG. 6. (Color online) Singly differential cross sections  $\sigma^{\text{SI}}(E_e)$  integrated over a forward cone with cone angle  $\theta_{\text{max}}$  at 10 keV (upper) and 100 keV (lower) antiproton energies. For an easier comparison, the cross sections were normalized to the maximum of the SDCS at  $\theta_{\text{max}} = 30^\circ$ . The wiggles in the 10 keV differential cross section are caused by partially resolved Beutler-Fano resonances due to doubly excited states which are excited by the projectile; see text.

to the maximum of the  $\theta_{\text{max}} = 30^\circ$  results for both 10 and 100 keV antiproton energy. At low projectile energies, the anticusp strongly suppresses the cross section near threshold ( $E_e \approx 0$ ) and the SDCS features a strong peak at  $\approx 30$  eV. This peak, extending from electron energies of 25 to 50 eV, also contains noticeable “wiggles”. They signify the interference between direct ionization and emission from autoionizing states. Such Beutler-Fano resonances have been, indeed, observed in  $p + \text{He}$  collisions [37]. It should be noted, however, that the fine-scale structure of these interferences can only be partially resolved by our numerical approach due to the finite propagation time before the spectrum is calculated. In order to fully resolve the Fano resonances integration over much longer time intervals corresponding to projectile distances  $R_z \gtrsim 10^4$  a.u. or alternative methods to calculate the electron spectra [38–40] would be needed. This is currently computationally not feasible for the problem at hand.

At high kinetic energies (100 keV) the anticusp causes a valley separating the near-threshold electrons from the binary-encounter peak. We note that the spectral shape (Fig. 6) is only weakly dependent on  $\theta_{\text{max}}$ . This indicates that, in future experiments, relatively large acceptance angles can be employed without smearing out the anticusp feature. The use of large electron collection angles will be advantageous since, due to the low electron emission probability in the forward direction and the low projectile flux, the rate of the ionization events near the forward direction is expected to be low. For example, while the shape of the energy differential cross sections with  $\theta_{\text{max}} = 5^\circ$  and  $\theta_{\text{max}} = 10^\circ$  is the same, the absolute magnitude of the  $\theta_{\text{max}} = 10^\circ$  cross section is nearly four times larger than that of the cross section for  $\theta_{\text{max}} = 5^\circ$ .

## V. CONCLUDING REMARKS

In this paper, we presented fully converged total cross sections for the single and double ionization of helium by antiproton impact over a wide range of impact energies calculated by directly solving the fully correlated six-dimensional TDSE. The present results show a better overall agreement with the experimental data [1–4] than other *ab initio* calculations [7–11, 13–16, 18]. We have also presented doubly differential cross sections for single ionization at 10 and 100 keV antiproton energies which were obtained by considering the fully correlated two-electron dynamics of the  $\text{He} + \bar{p}$  collisional system. In order to reach convergence for the differential cross section, a much larger angular basis set than for total cross sections is required with partial waves up to  $l_{\text{max}} = 5$ . For fully converged differential cross sections for DI, an even larger angular basis would be needed. We identified the presence of the anticusp and of the binary-encounter peak in the differential cross section, illustrating the importance of the postcollisional repulsion between the electron and the projectile at low impact energies. As a result of this repulsion, at 10 keV antiproton energy the electrons are “pushed” outside the binary-encounter peak and their emission in the forward direction is strongly suppressed. Finally, we showed that the direct measurement of the anticusp in the forward direction is possible even if the electrons are collected within a large solid angle.

## ACKNOWLEDGMENTS

This work was supported by a grant of the Romanian National Authority for Scientific Research (CNCS UEFIS-CDI) project number PN-II-ID-PCE-2011-3-0192, by the Hungarian Scientific Research Fund OTKA Nos. K103917 and NN 103279, by the Austrian Science Fund (FWF) under

SFB041 (VICOM) and SFB049 (NEXTLITE), and by the COST Action CM1204 (XLIC). J.F. acknowledges support by the NSF through a grant to ITAMP and by the European Research Council (ERC-2011-AdG Proposal No. 290981). The computational results presented were achieved by using the Vienna Scientific Cluster and through XSEDE resources provided under Grant No. TG-PHY090031.

- 
- [1] L. H. Andersen, P. Hvelplund, H. Knudsen, S. P. Møller, J. O. P. Pedersen, S. Tang-Petersen, E. Uggerhøj, K. Elsener, and E. Morenzoni, *Phys. Rev. A* **41**, 6536 (1990).
- [2] P. Hvelplund, H. Knudsen, U. Mikkelsen, E. Morenzoni, S. Møller, E. Uggerhøj, and T. Worm, *J. Phys. B: At., Mol. Opt. Phys.* **27**, 925 (1994).
- [3] H. Knudsen, H.-P. E. Kristiansen, H. D. Thomsen, U. I. Uggerhøj, T. Ichioka, S. P. Møller, C. A. Hunniford, R. W. McCullough, M. Charlton, N. Kuroda, Y. Nagata, H. A. Torii, Y. Yamazaki, H. Imao, H. H. Andersen, and K. Tökési, *Phys. Rev. Lett.* **101**, 043201 (2008).
- [4] H. Knudsen, H. P. E. Kristiansen, H. D. Thomsen, U. I. Uggerhøj, T. Ichioka, S. P. Møller, C. A. Hunniford, R. W. McCullough, M. Charlton, N. Kuroda, Y. Nagata, H. A. Torii, Y. Yamazaki, H. Imao, H. H. Andersen, and K. Tokesi, *Nucl. Instrum. Methods Phys. Res., Sect. B* **267**, 244 (2009).
- [5] K. Khayyat, T. Weber, R. Dörner, M. Achler, V. Mergel, L. Spielberger, O. Jagutzki, U. Meyer, J. Ullrich, R. Moshhammer, W. Schmitt, H. Knudsen, U. Mikkelsen, P. Aggerholm, E. Uggerhøj, S. P. Møller, V. D. Rodríguez, S. F. C. O'Rourke, R. E. Olson, P. D. Fainstein, J. H. McGuire, and H. Schmidt-Böcking, *J. Phys. B: At., Mol. Opt. Phys.* **32**, L73 (1999).
- [6] T. Kirchner and H. Knudsen, *J. Phys. B: At., Mol. Opt. Phys.* **44**, 122001 (2011).
- [7] M. Foster, J. Colgan, and M. S. Pindzola, *Phys. Rev. Lett.* **100**, 033201 (2008).
- [8] M. S. Pindzola, T. G. Lee, and J. Colgan, *J. Phys. B: At., Mol. Opt. Phys.* **44**, 205204 (2011).
- [9] X. Guan and K. Bartschat, *Phys. Rev. Lett.* **103**, 213201 (2009).
- [10] M. McGovern, D. Assafrão, J. R. Mohallem, C. T. Whelan, and H. R. J. Walters, *Phys. Rev. A* **79**, 042707 (2009).
- [11] I. B. Abdurakhmanov, A. S. Kadyrov, D. V. Fursa, I. Bray, and A. T. Stelbovics, *Phys. Rev. A* **84**, 062708 (2011).
- [12] P. D. Fainstein, V. H. Ponce, and R. D. Rivarola, *Phys. Rev. A* **36**, 3639 (1987).
- [13] A. Igarashi, A. Ohsaki, and S. Nakazaki, *Phys. Rev. A* **62**, 052722 (2000).
- [14] H. W. S. Sahoo and S. C. Mukherjee, *Nucl. Instrum. Methods Phys. Res., Sect. B* **233**, 318 (2005).
- [15] T. G. Lee, H. C. Tseng, and C. D. Lin, *Phys. Rev. A* **61**, 062713 (2000).
- [16] N. Henkel, M. Keim, H. J. Lüdde, and T. Kirchner, *Phys. Rev. A* **80**, 032704 (2009).
- [17] M. McGovern, D. Assafrão, J. R. Mohallem, C. T. Whelan, and H. R. J. Walters, *Phys. Rev. A* **81**, 032708 (2010).
- [18] M. Baxter and T. Kirchner, *Phys. Rev. A* **87**, 062507 (2013).
- [19] M. R. C. McDowell and J. P. Coleman, *Introduction to the Theory of Ion-Atom Collisions* (North-Holland Pub. Co, New York, 1970).
- [20] R. Abrines and I. C. Percival, *Proc. Phys. Soc., London* **88**, 861 (1966).
- [21] R. Abrines and I. C. Percival, *Proc. Phys. Soc., London* **88**, 873 (1966).
- [22] J. Feist, S. Nagele, R. Pazourek, E. Persson, B. I. Schneider, L. A. Collins, and J. Burgdörfer, *Phys. Rev. A* **77**, 043420 (2008).
- [23] B. I. Schneider and L. A. Collins, *J. Non-Cryst. Solids* **351**, 1551 (2005).
- [24] T. N. Rescigno and C. W. McCurdy, *Phys. Rev. A* **62**, 032706 (2000).
- [25] T. J. Park and J. C. Light, *J. Chem. Phys.* **85**, 5870 (1986).
- [26] B. I. Schneider, J. Feist, S. Nagele, R. Pazourek, S. Hu, L. A. Collins, and J. Burgdörfer, *Quantum Dynamic Imaging: Theoretical and Numerical Methods*, CRM Series in Mathematical Physics, edited by A. D. Bandrauk and M. Ivanov (Springer, New York, 2011), pp. 149–208.
- [27] K. Tökési and G. Hock, *J. Phys. B: At., Mol. Opt. Phys.* **29**, L119 (1996).
- [28] H. S. W. Massey, *Rep. Prog. Phys.* **12**, 248 (1949).
- [29] M. Gryziński, *Phys. Rev.* **115**, 374 (1959).
- [30] C. O. Reinhold and D. R. Schultz, *Phys. Rev. A* **40**, 7373 (1989).
- [31] K. Tökési, J. Wang, L. Gulyás, and J. Burgdörfer, *Hyperfine Interact.* **194**, 45 (2009).
- [32] A. Salin, *J. Phys. B: At. Mol. Phys.* **2**, 631 (1969).
- [33] G. B. Crooks and M. E. Rudd, *Phys. Rev. Lett.* **25**, 1599 (1970).
- [34] J. Macek, *Phys. Rev. A* **1**, 235 (1970).
- [35] R. G. Newton, *Scattering Theory of Waves and Particles* (Dover Publications Inc., Mineola, New York, 2002), p. 426.
- [36] G. Gamow, *Z. Phys. A* **52**, 510 (1929).
- [37] F. D. Schowengerdt and M. E. Rudd, *Phys. Rev. Lett.* **28**, 127 (1972).
- [38] C. W. McCurdy, M. Baertschy, and T. N. Rescigno, *J. Phys. B: At., Mol. Opt. Phys.* **37**, R137 (2004).
- [39] A. Palacios, T. N. Rescigno, and C. W. McCurdy, *Phys. Rev. A* **77**, 032716 (2008).
- [40] L. Argenti, R. Pazourek, J. Feist, S. Nagele, M. Liertzner, E. Persson, J. Burgdörfer, and E. Lindroth, *Phys. Rev. A* **87**, 053405 (2013).